COMMUNICATION

Highly Asymmetric n^+–p Heterojunction Quantum-Dot Solar Cells with Significantly Improved Charge-Collection Efficiencies

Min-Jae Choi, Sunchuel Kim, Hunhee Lim, Jaesuk Choi, Dong Min Sim, Soonmin Yim, Byung Tae Ahn, Jin Young Kim, and Yeon Sik Jung**

Due to their unique, size-dependent optical, electronic, and optoelectronic properties,[1–3] colloidal quantum dots (QDs) have attracted a great deal of attention for potentially widespread use in optoelectronic devices such as light-emitting diodes[4,5] and photodetectors.[6,7] In addition, colloidal QDs are solution processable at a low temperature,[8,9] and on this basis are also a promising candidate material system for low-cost, high-efficiency solar cells. With these advantages, there has been growing interest in QD solar cells (QDSCs) as next-generation photovoltaic devices.[10–13] Recently, QDSCs based on a depleted heterojunction structure, which consists of a wide band-gap n-type metal-oxide layer (e.g., TiO_2 and ZnO) and a p-type QD layer, were exploited to achieve significant improvement in power conversion efficiency (PCE).[14–16] Metal-oxide/QD heterojunction structures can appropriately locate the depletion region, where more efficient charge collection occurs with the aid of a built-in electric field, at the light-illuminated side. This structure can also effectively block hole injection from the QD layer by introducing a large valence band offset, thereby achieving more efficient charge collection.[14,15,17] The PCE of metal-oxide/QD heterojunction solar cells has reached ≈9.9%[18] by modifying QD surface passivation[19–21] and engineering device structures.[22–25]

Although there has been rapid progress in QDSCs, there remain challenges to be solved for further improvement of their energy conversion efficiency. One of the critical issues is the relatively short minority carrier diffusion length (typically several tens of nm) in the QD layer due to the high trap-state densities and low carrier mobility.[15,21,26] This seriously limits the optimum QD thickness of QDSCs, which is only slightly larger than the depletion region width of the QD film,[15,26] because an increase in the QD film thickness beyond the depletion region width significantly reduces the charge-collection efficiency. The small QD thickness is insufficient to fully absorb incident light, considering the absorption coefficient (≈10^4 cm^{-1}, near the band edge) of QD thin films,[27] and this limits the short-circuit current density (J_{sc}) and the overall performance of QDSCs. Therefore, increasing the depletion region width of QDSCs is very significant for utilizing a thicker QD layer without sacrificing the charge-collection efficiency.

Various approaches have been attempted to increase the optimal thickness of QD layer in QDSCs. For example, Ko et al. developed p–i–n heterojunction structures to extend the depletion region width by combining p–i and i–n junctions.[25] Yuan et al. reported a metal-oxide/p/p^+ structure based on graded doping of the QD layer, showing a superior charge-collection efficiency for the same QD layer thickness.[24] Recently, Crisp et al. showed that metal halide treatment on QD layer allows utilization of relatively thicker QD film in their devices while maintaining good charge-collection efficiency.[28] However, despite the significant role of metal oxides in the formation of n–p heterojunctions, systematic engineering of their electrical properties to maximize cell performance has not yet been carried out.

As shown in **Figure 1**a, conventional metal-oxide/QD heterojunction solar cells are composed of a lightly doped n-type metal-oxide layer (carrier density, $n \approx 10^{16}$–10^{17} cm^{-3}) and a p-type QD layer ($p \approx 10^{16}$–10^{17} cm^{-3}),[14,15,29,30] and thus the metal-oxide layer is also fully or partially depleted. It should be noted that the depleted metal-oxide layer does not provide a meaningful contribution to light absorption due to its wide energy band gap.[29] Thus, a strategy for extending the depletion region in the QD layer is more desirable. Because the ratio of the depletion region width in the QD to that in the metal oxide is inversely proportional to their doping-level ratio, the utilization of a heavily doped metal oxide would enable the formation of a highly extended depletion region in the QD layer (Figure 1b).

Here, we report that increasing the doping level of the metal oxide can significantly boost the depletion region width in the QD layer and improve the PCE of metal-oxide/QD heterojunction solar cells. The performance of ZnO/PbS QDSCs with a lightly doped ZnO (n-ZnO, $n \approx 10^{16}$ cm^{-3}) film or a heavily doped ZnO (n^+-ZnO, $n \approx 10^{19}$ cm^{-3}) layer was systematically characterized to elucidate the effect of the metal-oxide doping level. The introduction of n^+-ZnO instead of n-ZnO achieves an approximately 30% increase in the depletion region width

M.-J. Choi, S. Kim, H. Lim, J. Choi, D. M. Sim, S. Yim, Prof. B. T. Ahn, Prof. Y. S. Jung
Department of Materials Science and Engineering
Korea Advanced Institute of Science and Technology (KAIST)
291 Daehak-ro, Yuseong-gu
Daejeon 305-701, Republic of Korea
E-mail: ysjung@kaist.ac.kr
Dr. J. Y. Kim
Fuel Cell Research Center
Korea Institute of Science and Technology (KIST)
Seoul 136-791, Republic of Korea
E-mail: jinykim@kist.re.kr

DOI: 10.1002/adma.201503879

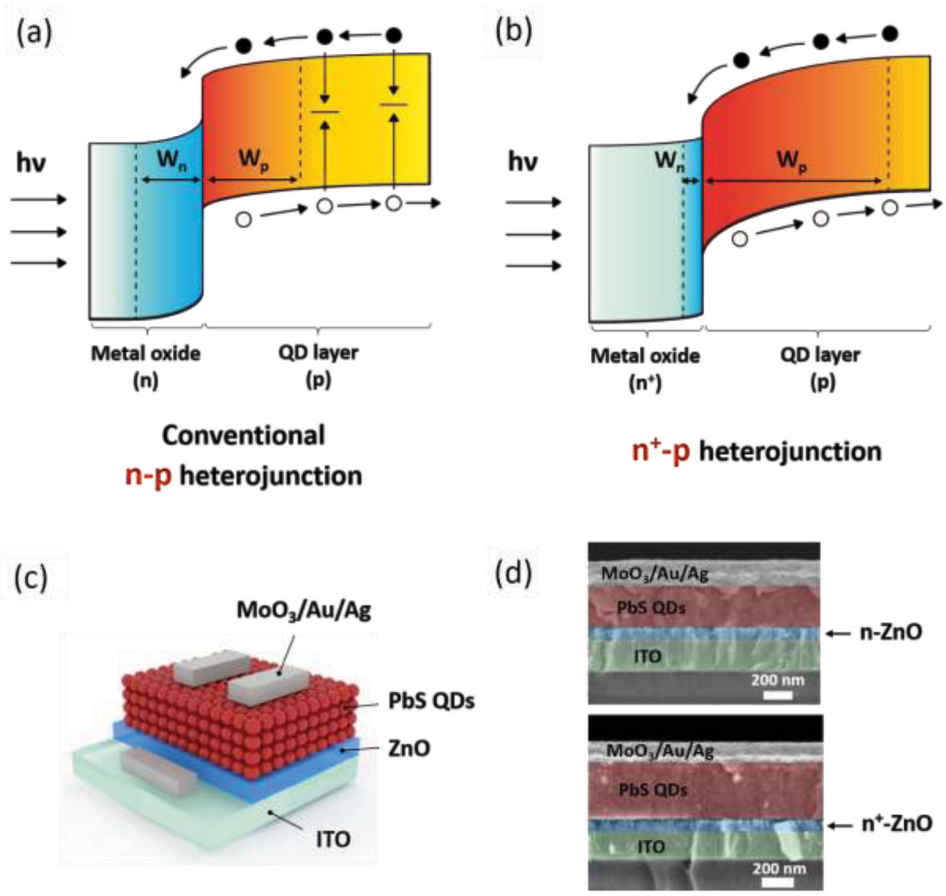

Figure 1. Schematic energy band diagram of a) conventional n–p heterojunction and b) n^+–p heterojunction QDSCs. W_n and W_p denote the depletion region width in the metal-oxide layer and QD layer, respectively. c) The device structure of ZnO/PbS heterojunction solar cells. d) False-color cross-section scanning electron microscopy (SEM) image of the n-ZnO/PbS and n^+-ZnO/PbS QDSCs.

in the QD layer from ≈186 to ≈242 nm, which was quantitatively estimated on the basis of current-density–voltage (*J*–*V*) characteristics and capacitance–voltage (*C*–*V*) measurements. The optimum thickness of the QD layer therefore also increases from ≈220 nm (n-ZnO device) to ≈300 nm (n^+-ZnO device). As a result, n^+-ZnO/PbS QDSCs demonstrate a maximum PCE of 7.55% and a J_{sc} of 23.5 mA cm^{-2}, which are significantly higher than those of n-ZnO/PbS QDSCs (PCE = 5.52%, and J_{sc} = 16.7 mA cm^{-2}). Furthermore, the highly conductive n^+-ZnO can have dual functionality as both a n-type layer and a transparent conducting oxide (TCO), and enables the successful fabrication and operation of QDSCs (PCE ≈ 7.33%) without an additional bottom indium tin oxide (ITO) layer typically used as a TCO.

In order to fabricate n-ZnO/PbS QDSCs (n–p heterojunction), a thin-film ZnO (thickness = 80 nm) was deposited onto an ITO/glass substrate from a ZnO target using radio-frequency (RF) sputter-deposition.[31] The carrier concentration of the ZnO film (n-ZnO) was measured to be ≈2.86 × 10^{16} cm^{-3}, which was estimated from the field-effect-transistor device characterization (see Table S1, Supporting Information). This value is in good agreement with other sputter-deposited ZnO thin films used in ZnO/PbS QDSCs.[15,31] PbS QDs with a first excitonic absorption peak at 930 nm (1.33 eV) were synthesized using a modified version of a method reported in the literature (see the Experimental Section for more details).[32] The PbS QDs were deposited onto the n-ZnO layer via sequential spin-casting and ligand exchange with 3-mercaptopropionic acid (MPA), as described previously.[32] The thickness of the QD layer was controlled by changing the number of QD casting iterations (unit QD thickness of 30–40 nm for one casting). The top metal electrode composed of MoO_3/Au/Ag was then deposited by thermal evaporation to form an Ohmic contact on the QD layer.[15,33] The scanning electron microscopy (SEM) image in Figure 1d shows the cross-sectional structure of the n-ZnO/PbS QDSCs. The energy band structure obtained from UV–vis absorbance spectra and ultraviolet photoelectron spectra (UPS) suggests the formation of an n–p junction at the ZnO/PbS QD interface (see more details in Figure S1 and S2, Supporting Information).

For fabricating the n^+-ZnO/PbS QDSCs (n^+–p heterojunction) with the structure depicted in Figure 1b, an n^+-ZnO layer was deposited onto an ITO/glass substrate by low-pressure chemical vapor deposition (LPCVD). LPCVD is an inexpensive and scalable technique that can be applied to achieve a conformal coating of high-quality oxide thin films with excellent purity.[34,35] The LPCVD process used for depositing n^+-ZnO provided a high deposition rate of 100 nm min^{-1}. The carrier

concentration of the n$^+$-ZnO layer was controlled by adjusting the flow rate of the n-type doping source (diborane, B_2H_6) from 0 to 20 sccm. Hall effect measurement results revealed that the carrier concentration of ZnO increased from 6.8×10^{18} cm^{-3} (0 sccm) to 2.5×10^{20} cm^{-3} (20 sccm) via the addition of B_2H_6 (see Table S2, Supporting Information). It should be noted that the ZnO film grown by LPCVD has a moderate n-type carrier concentration even without extrinsic doping, which can be explained by the oxygen nonstoichiometry and the introduction of hydrogen to the film during the LPCVD process.[36,37] The X-ray diffraction analysis results indicate that the samples have a wurtzite structure for both the ZnO and B:ZnO films, while the peaks of B:ZnO shifted slightly toward the larger angle side due to the boron doping (see more details in Figure S3, Supporting Information). Following the deposition of the n$^+$-ZnO layer, the same procedures as employed to fabricate n-ZnO/PbS QDSCs were implemented for the deposition of the QD layer and the metal electrode (Figure 1d). The QDSCs with the ZnO layer (10 sccm, B_2H_6), which provides a carrier concentration of 3.6×10^{19} cm^{-3}, showed the best cell performance, as presented in Figure S4 in the Supporting Information. The high carrier mobility and high conductivity of ZnO (10 sccm, B_2H_6) may improve the J_{sc} and fill factor (FF) of the device,[38] which will be discussed in more detail later in this paper. On the other hand, a significant decrease in the PCE was observed in the case of QDSCs with a more heavily doped ZnO film (20 sccm, B_2H_6). This can be attributed to the fact that that excessively heavy doping in the n$^+$-ZnO increased the defect density,[39,40] resulting in a decrease of device performance. Hereafter, we define n$^+$-ZnO as heavily boron-doped ZnO (10 sccm, B_2H_6) for convenience.

Figure 2a,b shows the *J*–*V* characteristics of n-ZnO/PbS ($n = 2.86 \times 10^{16}$ cm^{-3}) and n$^+$-ZnO/PbS QDSCs ($n = 3.6 \times 10^{19}$ cm^{-3}) depending on the thickness (t^{QD}) of the QD layer. The best efficiencies were obtained when t^{QD} were 220 and 300 nm for n-ZnO and n$^+$-ZnO QDSCs, respectively. (The performance parameters are summarized in Table S3 and S4 in the Supporting Information.) After t^{QD} exceeds this critical thickness, the PCE gradually decreases with increasing t^{QD}. In order to elucidate the effect of the n$^+$-ZnO layer more systematically, the performance parameters of n-ZnO/PbS and n$^+$-ZnO/PbS QDSCs were estimated and compared as a function of t^{QD} (Figure 2c). In both devices, a similar trend was observed; V_{oc} and FF decreased continuously with increasing t^{QD}, while J_{sc} increased up to a certain t^{QD} and decreased for a larger t^{QD}.

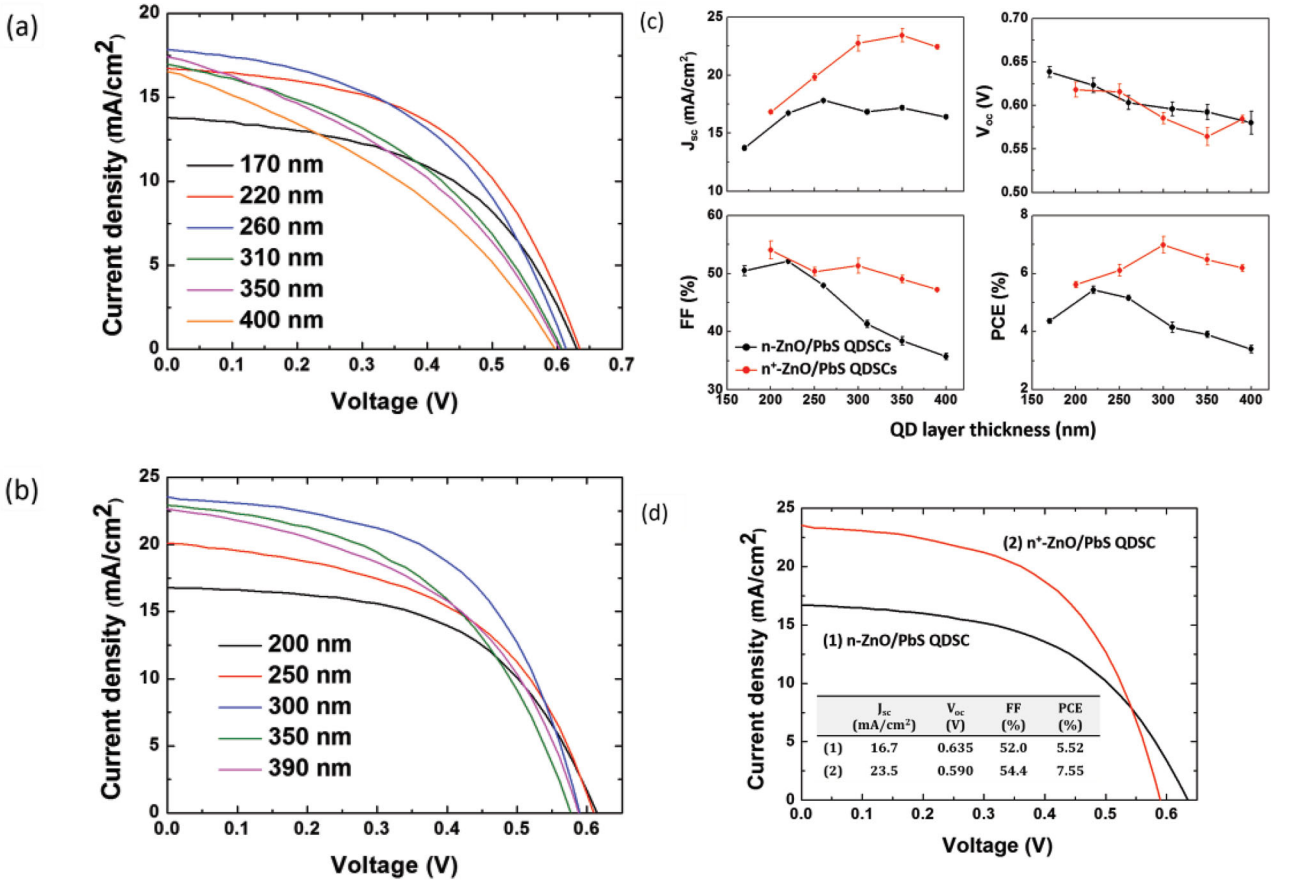

Figure 2. *J*–*V* characteristics of a) n-ZnO/PbS and b) n$^+$-ZnO/PbS QDSCs under AM1.5G illumination depending on the thickness of the QD layer. c) Performance characteristics of n-ZnO/PbS and n$^+$-ZnO/PbS QDSCs as a function of the QD layer thickness. The filled circles and error bars represent the average and standard deviation across four to six devices, respectively. (d) *J*–*V* characteristics of n-ZnO/PbS and n$^+$-ZnO/PbS QDSCs at optimum thickness of the QD layer.

However, these data exhibit two striking differences between n-ZnO/PbS and n$^+$-ZnO/PbS QDSCs. First, the J_{sc} value is maximized at t^{QD} = 260 nm in the n-ZnO/PbS QDSCs, while that of n$^+$-ZnO/PbS QDSCs continuously increases until t^{QD} reaches 350 nm. Second, the FF of n-ZnO/PbS QDSCs rapidly decreases after t^{QD} exceeds 220 nm, but in the case of n$^+$-ZnO/PbS QDSCs, the FF is maintained at a similar value until t^{QD} = 300 nm. As a result, the optimum t^{QD} of the n$^+$-ZnO/PbS QDSCs increased to 300 nm from 220 nm for the n-ZnO/PbS QDSCs. These results strongly suggest a substantial increase of the depletion region width in the QD layer, allowing the utilization of a thicker QD layer in the n$^+$-ZnO/PbS QDSCs. When the QD layer is fully depleted, efficient charge collection across the entire thickness of the QD layer is achieved with the aid of the built-in electric field,[25] resulting in an increase of J_{sc} with increasing t^{QD}. However, after t^{QD} exceeds the depletion region width in the QD layer, the charge-collection efficiency rapidly decreases with increasing t^{QD} due to the insufficient minority carrier diffusion length in the QD layer.[26] Thus, there is no further increase in J_{sc} with increasing t^{QD} despite the increase of the total light absorbance of the QD layer. Moreover, the FF of the QDSCs rapidly decreases with an increase of t^{QD} due to an increase of the series resistance (R_s) and a decrease of the shunt resistance (R_{sh}) (see Figure S5, Supporting Information). This can be attributed to an increase of the quasi-neutral region making the QD film more resistive[25] and causing leakage in the film.

In this study, a similar enhancement of device performance was observed when the n-ZnO layer was annealed at 300 °C in an N_2-filled glove box before use. The n-type carrier concentration of ZnO thin films can be raised by annealing in an inert atmosphere due to the increase of the oxygen vacancy concentration[41,42] (see Table S1, Supporting Information). We found that the PCE of the n-ZnO/PbS devices (t^{QD} = 280 nm) increased from 4.43% (no annealing; n-ZnO) to 4.91% (inert annealing for 30 min) and 5.31% (inert annealing for 60 min) based on collective improvements in the J_{sc} and FF (Figure S6, Supporting Information). Because the t^{QD} of the devices is higher than the depletion region width of the QD film, the improved performance may originate from the extension of the depletion region width of the QD film by increasing the n-type carrier concentration of ZnO. However, a significant difference was not observed in the case of air annealing, which did not increase the carrier concentration. These results also support that increasing the n-type carrier concentration of the ZnO layer extends the depletion region width in the QD layer.

From the *J–V* characteristics at the optimum t^{QD} the n$^+$-ZnO/PbS QDSCs exhibit a PCE of 7.55%, which corresponds to a 37% improvement from that of n-ZnO/PbS QDSCs (Figure 2d). Most of the improvement was achieved from the enhancement of J_{sc} (almost a 41% increase), which can be explained by the increased optimum t^{QD} in the n$^+$-ZnO/PbS QDSCs. An atomic force microscopy (AFM) analysis provided similar surface roughness levels for thin n-ZnO and n$^+$-ZnO films, indicating that surface roughness is not an important factor for the improved photocurrent (Figure S7, Supporting Information). In addition, the external quantum efficiency and internal quantum efficiency data show that more charge carriers are extracted in n$^+$-ZnO/PbS QDSCs (Figure S8, Supporting Information). The FF of the n$^+$-ZnO/PbS QDSCs also records a 4.6% higher value compared to the n-ZnO/PbS QDSCs in spite of the relatively thicker QD layer of the former. This can be attributed to the smaller R_s, owing to the five orders-of-magnitude higher conductivity of n$^+$-ZnO relative to that of n-ZnO. On the other hand, the n$^+$-ZnO/PbS QDSCs showed a relatively smaller V_{oc} (7% decrease) compared to the n-ZnO/PbS QDSCs. Earlier turn-on points of the n$^+$-ZnO/PbS QDSCs in the dark current curves under forward bias (Figure S9, Supporting Information) suggest more charge recombination compared to the n-ZnO/PbS QDSCs.[43,44] The high carrier concentration of the n$^+$-ZnO layer and its relatively thicker QD layer may promote the interface and bulk recombination, respectively, leading to a decrease in V_{oc}.[17,25] This is in good agreement with the result (shown in Figure S4, Supporting Information) that the V_{oc} of n$^+$-ZnO/PbS QDSCs decreases with increasing carrier density of n$^+$-ZnO. It was previously reported that the addition of dopants to ZnO produced defect states,[39,40] which promoted interface recombination at ZnO/PbS. However, the degree of V_{oc} decrease is considerably smaller compared to the increase of J_{sc}.

For the quantitative characterization of the depletion region width, we carried out C-V measurement of the devices with various t^{QD} values. The ZnO/PbS QDSCs can be modelled as a parallel-plate capacitor in series,[26] in which the dielectric thickness of each capacitor corresponds to the depletion region width of ZnO and PbS QD layer, respectively. **Figure 3**a shows the change of the capacitance values at zero-bias as a function of t^{QD} for both n-ZnO/PbS and n$^+$-ZnO/PbS QDSCs (more data are displayed in Figure S10, Supporting Information). It should be noted that the capacitance of the n$^+$-ZnO/PbS QDSCs is relatively larger than those of n-ZnO/PbS QDSCs at the same t^{QD}. This is because the significantly smaller depletion region width in the n$^+$-ZnO layer resulting from its three orders-of-magnitude higher n-type carrier density leads to a higher capacitance value compared to that of n-ZnO. For both devices, the capacitance decreases with increasing t^{QD} up to a certain t^{QD} and becomes relatively constant. When t^{QD} is small enough to be fully depleted, the capacitance decreases with increasing t^{QD} due to an increase of the dielectric thickness.[26] However, if t^{QD} exceeds the maximum depletion region width of QD film, the devices show almost constant capacitance. Figure 3a shows that the capacitance values of n-ZnO/PbS and n$^+$-ZnO/PbS QDSCs become saturated after t^{QD} reaches 220 nm and 300 nm, respectively. This difference suggests that the depletion region width in the QD layer is extended in the n$^+$-ZnO/PbS QDSCs, which is in good agreement with the *J–V* characterization results in Figure 2.

Furthermore, we calculated the depletion region width in the QD layer of the devices by deriving the carrier concentration and the dielectric constant of the QD layer. First, we measured the *C–V* curve of n$^+$-ZnO/PbS QDSC (t^{QD} = 180 nm) to obtain the relative permittivity of the QD layer (Figure 3b). The capacitance of the device can be expressed as:[45]

$$C = \frac{\varepsilon_{QD}\varepsilon_0}{d} A \quad (1)$$

where ε_{QD}, ε_0, A, and d are the dielectric constant of the QD layer, the vacuum permittivity, the device area, and the dielectric

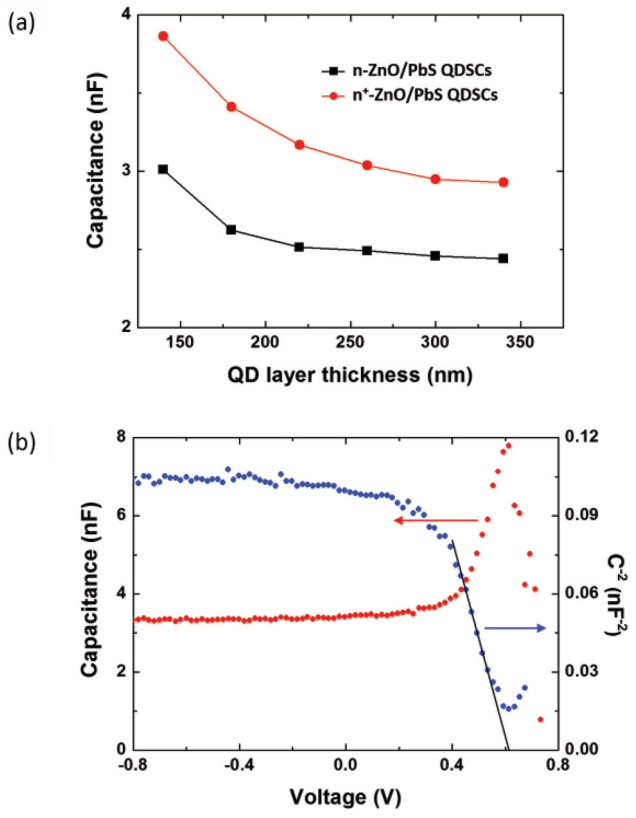

Figure 3. a) Capacitance values of n-ZnO/PbS and n^+-ZnO/PbS QDSCs at zero-bias as a function of the QD layer thickness. b) Capacitance–voltage measurement and Mott–Schottky plots of fully depleted n^+-ZnO/PbS QDSCs (t^{QD} = 180 nm).

thickness, respectively. Because t^{QD} is small enough to be fully depleted and the carrier concentration of the n^+-ZnO layer is much higher than that of the QD layer, d is almost equal to t^{QD} (d = 180 nm). By using the reverse-biased capacitance (3.45 nF), ε_{QD} is estimated to be 19.8 from Equation (1). We then performed a Mott–Schottky analysis of the same device as shown, in Figure 3b. The carrier concentration of the QD layer, N_a, is given by:[15,29]

$$N_a = \frac{2}{A^2 q \varepsilon_{QD} \varepsilon_0 \frac{d}{dV}\left(\frac{1}{C^2}\right)} \quad (2)$$

where q is the elementary charge. The slope of the Mott–Schottky plot in the linear regime was evaluated and substituted in Equation (2) to yield $N_a = 2.26 \times 10^{16}$ cm^{-3}. This value is comparable with those reported for MPA-treated PbS QD films.[46] The depletion region width in the QD layer at zero-bias, W_p, can be established by:[29]

$$W_p = \frac{1}{N_a}\left[\frac{2\varepsilon_{QD}\varepsilon_0}{q\left(\frac{1}{N_a}+\frac{1}{N_d}\right)}V_{bi}\right]^{\frac{1}{2}} \quad (3)$$

where N_d and V_{bi} are the carrier concentration of the metal-oxide layer and the built-in voltage, respectively. The V_{bi} of the QDSCs was obtained from the crossover point between the light and dark J–V characteristics,[9,15] which was 0.638 and 0.605 V for n-ZnO/PbS and n^+-ZnO/PbS QDSCs, respectively. From Equation (3), W_p for n-ZnO/PbS and n^+-ZnO/PbS QDSCs was calculated as 186 and 242 nm, respectively. Comparison of the calculated values to the optimum QD thickness from the experimental data suggests that W_p was significantly extended in the n^+-ZnO/PbS QDSCs.

TCOs are another important component of solar cells because their performance is highly dependent on the electrical, optical, and surface properties of TCOs.[38,47] ITO-coated glass substrates have been widely used as TCOs in QDSCs owing to their high transparency and conductivity. However, the cost of ITO substrates is high and continuously increasing because of the limited indium reserves.[48,49] Therefore, replacing ITO with alternative low-cost TCO materials is beneficial for further reduction of the material cost of QDSCs. B:ZnO grown by LPCVD can be considered an alternative to ITO due to its high conductivity and mobility, as well as low cost and high throughput.[50,51] Furthermore, the LPCVD-grown B:ZnO thin films have highly textured as-grown surface morphologies without any etching treatments, which can contribute to considerable light scattering and light trapping in solar cells.[52]

To fabricate ITO-free QDSCs, we deposited thicker B:ZnO thin films on bare glass substrates, as shown in **Figure 4**a. The high deposition rate (≈100 nm min^{-1}) of LPCVD allows the rapid formation of relatively thick films. In this manner, the stack structure of QDSCs can be simplified as glass/B:ZnO/QD/metal without the need of depositing additional TCO films. As the thickness of the B:ZnO film increased, the B:ZnO film presented a pyramid-like, highly textured structure due to the increased grain size (Figure S11, Supporting Information). In addition, the electrical properties of the B:ZnO films were also correlated with the thickness of the B:ZnO film (see Table S6, Supporting Information). The increased grain size of B:ZnO would decrease the grain boundary density of the film and consequently reduce the effect of carrier scattering at grain boundaries. Because the transport of electrons in polycrystalline B:ZnO is dominated by the carrier scattering effect at the grain boundaries when the carrier concentration is lower than 1×10^{20} cm^{-3}, the increased grain size of B:ZnO has contributed to the improvement of the carrier mobility and the conductivity of the film.[53] To explore the relationship between the thickness of the B:ZnO film and the QDSC device performance, B:ZnO films with three different thickness (450, 850, and 1400 nm) were used to fabricate ITO-free QDSCs (see Figure S12, Supporting Information). Figure S12 shows that the ITO-free QDSCs worked normally, confirming that the B:ZnO film serves not only as an n-type layer, but also as a TCO. The ITO-free QDSCs exhibited the highest PCE when the thickness of the B:ZnO film was 850 nm. For thin B:ZnO films, the relatively high sheet resistance may cause a decrease of J_{sc} and FF. For excessively thick B:ZnO films, the J_{sc} value decreases although the film shows a relatively high haze factor (Figure S9, Supporting Information). This can be attributed to the significant transmittance loss of the film due to the free carrier absorption. In addition, the small degree of light scattering mostly occurs within the short-wavelength range (400–600 nm),

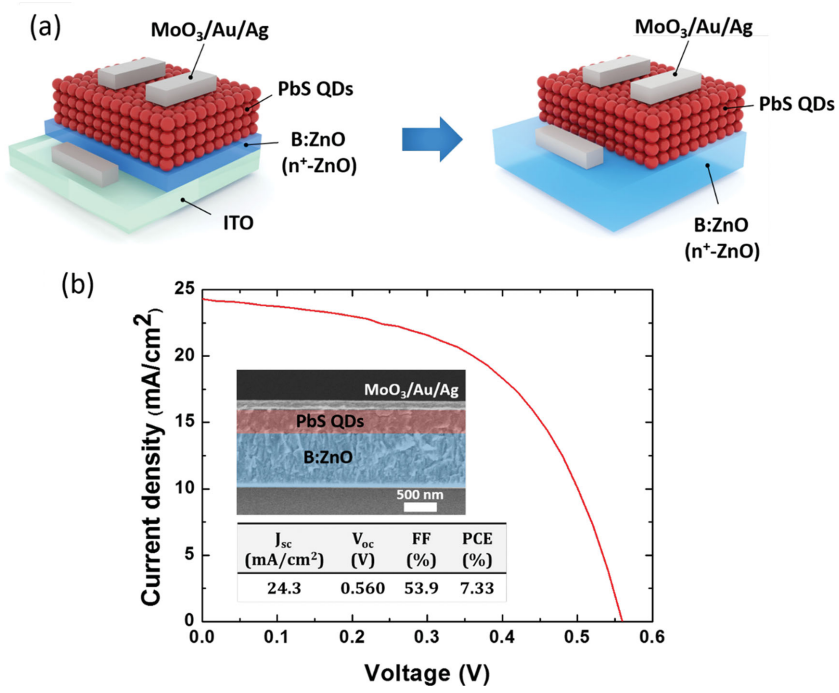

Figure 4. ITO-free QDSCs fabricated on B:ZnO/glass substrates. a) Device structure with and without ITO layer. b) *J–V* characteristics of QDSCs fabricated on an 850 nm thick B:ZnO film under AM1.5G illumination. The inset data present a cross-sectional SEM image and the performance of the device.

where most of the incident light can already be absorbed within the QD film due to sufficiently high absorption coefficients. Figure 4b shows the *J–V* characteristics of the best ITO-free QDSCs, which exhibit a J_{sc} of 24.3 mA cm^{-2}, a V_{oc} of 0.560 V, an FF of 53.9%, and a PCE of 7.33%. This efficiency is very close to that of the n^+-ZnO/PbS QDSC with a bottom ITO TCO film, suggesting additional possibilities of ITO-free QDSCs. We also performed *J–V* measurement of ITO-free QDSCs as a function of t^{QD} (Figure S13, Supporting Information). The results indicate that ITO-free QDSCs show the best performance when t^{QD} = 320 nm, which is consistent with the case of the n^+-ZnO/PbS QDSCs shown above.

To summarize, we introduced a new approach to considerably extend the depletion region width in the QD layer of metal-oxide/QD heterojunction solar cells by employing heavily boron-doped n^+-ZnO. This methodology effectively increased the depletion region width in the p-type QD layer by 30% compared to the counterpart with a conventional n-ZnO with a low carrier concentration. Consequently, the thickness-optimized n^+-ZnO/PbS QDSCs recorded a PCE of 7.55%, which is 37% higher than that of the n-ZnO/PbS QDSCs. Furthermore, we reported that the heavily doped ZnO can also function as a practical TCO by demonstrating the successful fabrication and operation of ITO-free QDSCs (PCE ≈ 7.33%). This heavy doping strategy would be also effective for solution-based metal-oxide synthesis for reduction of processing cost, which remains as future work. Moreover, it is expected that our approach can be combined with the recent innovations of QD surface passivation and architecture engineering to further improve the energy conversion efficiency of QDSCs. We also believe this study may provide new opportunities in QD-based optoelectronic devices where engineering of the depletion region is highly beneficial.

Experimental Section

Materials and Synthesis of PbS Quantum Dots: Lead(II) oxide powder (PbO) (99%), 1-octadecene (ODE) (technical grade 90%), oleic acid (OA) (technical grade 90%), oleylamine (OLA) (technical grade 70%), hexamethyldisilathiane ($(TMS)_2S$) (synthesis grade), cadmium chloride ($CdCl_2$) (99.99%), and MPA (99%) were purchased from Sigma-Aldrich and used without further purification. PbS QDs with a first exciton absorption peak at 930 nm (1.33 eV) were synthesized using a modified version of a method reported in the literature.[30] Details of the synthesis are described in the Supporting Information.

Fabrication of ZnO Films: The n-ZnO films were sputter-deposited at a rate of 0.13 Å s^{-1} with 60 W RF power (0.47 W cm^{-2}) under an atmosphere of 20 mTorr Ar and 1 mTorr O_2. The B:ZnO layer was deposited on ITO/glass or bare glass substrates at 200 °C using a low-pressure hot-wall system operated under chemical vapor deposition conditions (NCD Tech.). The substrates were sonicated in Triton X-100 aqueous solution (3% volume ratio), deionized (DI) water, and 2-propanol prior to deposition. Diethylzinc vapor (flow rate = 200 sccm) and water vapor (150 sccm), as the zinc and oxygen source, respectively, were supplied with Ar carrier gas. The working pressure was set to 5 Torr during the deposition process. Diborane (flow rate = 0–20 sccm) was added for n-type doping of ZnO. The SEM results indicated that 10 min of deposition produced a B:ZnO film with ≈1 µm thickness. The B:ZnO films were annealed at 300 °C for 30 min on a hot plate in air before use.

Fabrication of Quantum-Dot Solar-Cell Devices: All fabrication steps were performed in a fume hood. The PbS QD layer was produced via sequential spin-casting and ligand exchange using MPA. For the formation of the unit QD layer with a thickness of 30–40 nm, QD solutions with a concentration of 60 mg mL^{-1} were spin-casted on the ZnO layer. The deposited QD layer was then immersed in 1% v/v MPA in methanol solution for 3 s, followed by spinning for drying. The samples were then washed with methanol to remove unbound ligands. All of the spin-casting process was done at a speed of 2500 rpm. The top metal electrode composed of MoO_3 (15 nm), Au (40 nm), and Ag (120 nm) was deposited using thermal evaporation at a pressure of 3×10^{-6} Torr. The active device area (3.14 mm^2) was determined by the overlapped area between the ITO and the metal electrode. Devices with a larger active area (10 mm^2) are also demonstrated in Figure S14 in the Supporting Information, and they show the same improvement trends for J_{sc} and PCE despite slightly lower performance.

Characterizations: UV–vis absorption spectra of PbS QDs were measured using a UV–vis spectrophotometer (Mecasys, Optizen POP, Korea). The surface morphologies of the B:ZnO layer and cross-section images of QDSCs were observed using a field emission scanning electron microscope (FE-SEM, Hitachi, S-4800). Capacitance–voltage (CV) characterization was performed in a N_2-filled glove box in a voltage sweep range of –1 and +1 V (a step size of 0.020 V). The amplitude and the frequency of the AC signal were set to 25 mV and 500 Hz. UPS data were obtained using an He lamp at 21.2 eV incorporated into an ultrahigh vacuum chamber with a base pressure of 10^{-10} Torr. A –10.0 V bias was applied to the samples for accurate calibration. The current–voltage (*J–V*)

characteristics were obtained using a Keithley 2450 source meter in an N_2-filled glove box. *J–V* sweeps were performed between –1 and +1 V, with a step size of 0.020 V. The devices were illuminated through the glass substrate using a 150 W Xe lamp with an AM1.5G filter (LS-150-Xe, Abet Technologies). The light intensity was calibrated to 100 mW cm^{-2} using an Si reference cell (BS-520, Bunko Keiki).

Supporting Information

Supporting Information is available from the Wiley Online Library or from the author.

Acknowledgements

This work was supported by the Center for Advanced Meta-Materials (CAMM; No. 2014M3A6B3063707) funded by the Ministry of Science, ICT and Future Planning as Global Frontier Project and by the Basic Science Research Program (NRF-2013R1A1A2061440). This work was also supported by Open Innovation Lab Project from National Nanofab Center (NNFC).

Received: August 10, 2015
Revised: September 24, 2015
Published online: December 21, 2015

[1] M. A. Hines, G. D. Scholes, *Adv. Mater.* **2003**, *15*, 1844.
[2] H. Choi, J. H. Ko, Y. H. Kim, S. Jeong, *J. Am. Chem. Soc.* **2013**, *135*, 5278.
[3] Y. Liu, M. Gibbs, J. Puthussery, S. Gaik, R. Ihly, H. W. Hillhouse, M. Law, *Nano Lett.* **2010**, *10*, 1960.
[4] J. S. Steckel, S. Coe-Sullivan, V. Bulovic, M. G. Bawendi, *Adv. Mater.* **2003**, *15*, 1862.
[5] G. Konstantatos, C. J. Huang, L. Levina, Z. H. Lu, E. H. Sargent, *Adv. Funct. Mater.* **2005**, *15*, 1865.
[6] G. Konstantatos, I. Howard, A. Fischer, S. Hoogland, J. Clifford, E. Klem, L. Levina, E. H. Sargent, *Nature* **2006**, *442*, 180.
[7] K. K. Manga, J. Z. Wang, M. Lin, J. Zhang, M. Nesladek, V. Nalla, W. Ji, K. P. Loh, *Adv. Mater.* **2012**, *24*, 1697.
[8] J. M. Luther, M. Law, Q. Song, C. L. Perkins, M. C. Beard, A. J. Nozik, *ACS Nano* **2008**, *2*, 271.
[9] J. M. Luther, M. Law, M. C. Beard, Q. Song, M. O. Reese, R. J. Ellingson, A. J. Nozik, *Nano Lett.* **2008**, *8*, 3488.
[10] X. H. Wang, G. I. Koleilat, J. Tang, H. Liu, I. J. Kramer, R. Debnath, L. Brzozowski, D. A. R. Barkhouse, L. Levina, S. Hoogland, E. H. Sargent, *Nat. Photonics* **2011**, *5*, 480.
[11] J. J. Choi, W. N. Wenger, R. S. Hoffman, Y. F. Lim, J. Luria, J. Jasieniak, J. A. Marohn, T. Hanrath, *Adv. Mater.* **2011**, *23*, 3144.
[12] P. K. Santra, P. V. Kamat, *J. Am. Chem. Soc.* **2013**, *135*, 877.
[13] M. J. Choi, J. Oh, J. K. Yoo, J. Choi, D. M. Sim, Y. S. Jung, *Energy Environ. Sci.* **2014**, *7*, 3052.
[14] A. G. Pattantyus-Abraham, I. J. Kramer, A. R. Barkhouse, X. H. Wang, G. Konstantatos, R. Debnath, L. Levina, I. Raabe, M. K. Nazeeruddin, M. Gratzel, E. H. Sargent, *ACS Nano* **2010**, *4*, 3374.
[15] P. R. Brown, R. R. Lunt, N. Zhao, T. P. Osedach, D. D. Wanger, L. Y. Chang, M. G. Bawendi, V. Bulovic, *Nano Lett.* **2011**, *11*, 2955.
[16] D. A. R. Barkhouse, R. Debnath, I. J. Kramer, D. Zhitomirsky, A. G. Pattantyus-Abraham, L. Levina, L. Etgar, M. Gratzel, E. H. Sargent, *Adv. Mater.* **2011**, *23*, 3134.
[17] B. Ehrler, K. P. Musselman, M. L. Bohm, F. S. F. Morgenstern, Y. Vaynzof, B. J. Walker, J. L. MacManus-Driscoll, N. C. Greenham, *ACS Nano* **2013**, *7*, 4210.
[18] National Renewable Energy Laboratory (NREL), Best Research–cell Efficiencies, http://www.nrel.gov/ncpv/images/efficiency_chart.jpg; Accessed: November, 2015.
[19] A. H. Ip, S. M. Thon, S. Hoogland, O. Voznyy, D. Zhitomirsky, R. Debnath, L. Levina, L. R. Rollny, G. H. Carey, A. Fischer, K. W. Kemp, I. J. Kramer, Z. J. Ning, A. J. Labelle, K. W. Chou, A. Amassian, E. H. Sargent, *Nat. Nanotechnol.* **2012**, *7*, 577.
[20] I. Veremchuk, I. Antonyshyn, C. Candolfi, X. Feng, U. Burkhardt, M. Baitinger, J. T. Zhao, Y. Grin, *Inorg. Chem.* **2013**, *52*, 4458.
[21] D. Zhitomirsky, O. Voznyy, L. Levina, S. Hoogland, K. W. Kemp, A. H. Ip, S. M. Thon, E. H. Sargent, *Nat. Commun.* **2014**, *5*, 3803.
[22] C. H. M. Chuang, P. R. Brown, V. Bulovic, M. G. Bawendi, *Nat. Mater.* **2014**, *13*, 796.
[23] I. J. Kramer, L. Levina, R. Debnath, D. Zhitomirsky, E. H. Sargent, *Nano Lett.* **2011**, *11*, 3701.
[24] M. J. Yuan, D. Zhitomirsky, V. Adinolfi, O. Voznyy, K. W. Kemp, Z. J. Ning, X. Z. Lan, J. X. Xu, J. Y. Kim, H. P. Dong, E. H. Sargent, *Adv. Mater.* **2013**, *25*, 5586.
[25] D. K. Ko, P. R. Brown, M. G. Bawendi, V. Bulovic, *Adv. Mater.* **2014**, *26*, 4845.
[26] L. Y. Chang, R. R. Lunt, P. R. Brown, V. Bulovic, M. G. Bawendi, *Nano Lett.* **2013**, *13*, 994.
[27] Z. Hens, I. Moreels, *J. Mater. Chem.* **2012**, *22*, 10406.
[28] R. W. Crisp, D. M. Kroupa, A. R. Marshall, E. M. Miller, J. B. Zhang, M. C. Beard, J. M. Luther, *Sci. Rep.* **2015**, *5*, 9945.
[29] S. M. Willis, C. Cheng, H. E. Assender, A. A. R. Watt, *Nano Lett.* **2012**, *12*, 1522.
[30] G. H. Kim, B. Walker, H. B. Kim, J. Y. Kim, E. H. Sargent, J. Park, J. Y. Kim, *Adv. Mater.* **2014**, *26*, 3321.
[31] K. S. Leschkies, T. J. Beatty, M. S. Kang, D. J. Norris, E. S. Aydil, *ACS Nano* **2009**, *3*, 3638.
[32] P. Maraghechi, A. J. Labelle, A. R. Kirmani, X. Z. Lan, M. M. Adachi, S. M. Thon, S. Hoogland, A. Lee, Z. J. Ning, A. Fischer, A. Amassian, E. H. Sargent, *ACS Nano* **2013**, *7*, 6111.
[33] J. B. Gao, C. L. Perkins, J. M. Luther, M. C. Hanna, H. Y. Chen, O. E. Semonin, A. J. Nozik, R. J. Ellingson, M. C. Beard, *Nano Lett.* **2011**, *11*, 3263.
[34] W. Kern, G. L. Schnable, *IEEE Trans. Electron Devices* **1979**, *26*, 647.
[35] N. Rausch, E. P. Burte, *J. Electrochem. Soc.* **1993**, *140*, 145.
[36] J. Bang, K. J. Chang, *Appl. Phys. Lett.* **2008**, *92*, 132109.
[37] X. L. Chen, B. H. Xu, J. M. Xue, Y. Zhao, C. C. Wei, J. Sun, Y. Wang, X. D. Zhang, X. H. Geng, *Thin Solid Films* **2007**, *515*, 3753.
[38] D. H. Wang, A. K. K. Kyaw, V. Gupta, G. C. Bazan, A. J. Heeger, *Adv. Energy Mater.* **2013**, *3*, 1161.
[39] A. J. Wang, T. F. Chen, S. H. Lu, Z. L. Wu, Y. L. Li, H. Chen, Y. S. Wang, *Nanoscale Res. Lett.* **2015**, *10*, 1.
[40] V. Kumar, R. G. Singh, L. P. Purohit, R. M. Mehra, *J. Mater. Sci. Technol.* **2011**, *27*, 481.
[41] L. Lu, M. Wong, *IEEE Trans. Electron Devices* **2014**, *61*, 1077.
[42] H. W. Park, K. B. Chung, J. S. Park, *Curr. Appl. Phys.* **2012**, *12*, S164.
[43] N. Zhao, T. P. Osedach, L. Y. Chang, S. M. Geyer, D. Wanger, M. T. Binda, A. C. Arango, M. G. Bawendi, V. Bulovic, *ACS Nano* **2010**, *4*, 3743.
[44] K. W. Kemp, A. J. Labelle, S. M. Thon, A. H. Ip, I. J. Kramer, S. Hoogland, E. H. Sargent, *Adv. Energy Mater.* **2013**, *3*, 917.
[45] J. Tang, L. Brzozowski, D. A. R. Barkhouse, X. H. Wang, R. Debnath, R. Wolowiec, E. Palmiano, L. Levina, A. G. Pattantyus-Abraham, D. Jamakosmanovic, E. H. Sargent, *ACS Nano* **2010**, *4*, 869.
[46] K. S. Jeong, J. Tang, H. Liu, J. Kim, A. W. Schaefer, K. Kemp, L. Levina, X. H. Wang, S. Hoogland, R. Debnath, L. Brzozowski, E. H. Sargent, J. B. Asbury, *ACS Nano* **2012**, *6*, 89.

[47] M. M. Adachi, A. J. Labelle, S. M. Thon, X. Lan, S. Hoogland, E. H. Sargent, *Sci. Rep.* **2013**, *3*.
[48] A. R. Rathmell, B. J. Wiley, *Adv. Mater.* **2011**, *23*, 4798.
[49] Y. J. Xia, J. Y. Ouyang, *J. Mater. Chem.* **2011**, *21*, 4927.
[50] J. C. Hsiao, C. H. Chen, H. J. Yang, C. L. Wu, C. M. Fan, C. F. Huang, C. C. Lin, P. C. Yu, J. C. Hwang, *J. Taiwan Inst. Chem. Eng.* **2013**, *44*, 758.
[51] S. Fay, J. Steinhauser, S. Nicolay, C. Ballif, *Thin Solid Films* **2010**, *518*, 2961.
[52] S. Nicolay, M. Despeisse, F. J. Haug, C. Ballif, *Sol. Energy Mater. Sol. Cells* **2011**, *95*, 1031.
[53] S. Fay, J. Steinhauser, S. Nicolay, C. Ballif, *Thin Solid Films* **2010**, *518*, 2961.